The Astrophysical Journal, 845:19 (13pp), 2017 August 10 https://doi.org/10.3847/1538-4357/aa7de7

New Improved Indirect Measurement of the $^{19}F(p, \alpha)^{16}O$ Reaction at Energies of Astrophysical Relevance

I. Indelicato[1], M. La Cognata[1], C. Spitaleri[1,2], V. Burjan[3], S. Cherubini[1,2], M. Gulino[1,4], S. Hayakawa[5], Z. Hons[3], V. Kroha[3], L. Lamia[1], M. Mazzocco[6,7], J. Mrazek[3], R. G. Pizzone[1], S. Romano[1,2], E. Strano[6,7], D. Torresi[6,7], and A. Tumino[1,4]
[1] INFN, Laboratori Nazionali del Sud, Catania, Italy; indelicato@lns.infn.it
[2] Dipartimento di Fisica e Astronomia dell'Università degli studi di Catania, Catania, Italy
[3] Nuclear Physics Institute of ASCR, Rez near Prague, Czech Republic
[4] Università degli studi di Enna Kore, Enna, Italy
[5] RIKEN, CNS, 2-1 Hirosawa, Wako, Saitama 351-0198, Japan
[6] INFN, Sezione di Padova, Padova, Italy
[7] Dipartimento di Fisica dell'Università di Padova, Padova, Italy
Received 2017 May 30; revised 2017 July 3; accepted 2017 July 3; published 2017 August 8

Abstract

Fluorine abundance determination is of great importance in stellar physics to understand s-elements production and mixing processes in asymptotic giant branch (AGB) stars. Up to now, theoretical models overproduce F abundances in AGB stars with respect to the observed values, thus calling for further investigation of the reactions involving fluorine. In particular, the $^{19}F(p, \alpha)^{16}O$ reaction is the main destruction channel of fluorine at the bottom of the convective envelope in AGB stars, an H-rich environment where it can experience temperatures high enough to determine its destruction, owing to additional mixing processes. In this paper the Trojan horse method (THM) was used to extract the $^{19}F(p, \alpha_0)^{16}O$ S-factor in the energy range of astrophysical interest ($E_{cm} \approx 0$–1 MeV). This is the most relevant channel at the low temperatures (few 10^7 K) characterizing the bottom of the convective envelope, according to current knowledge. A previous indirect experiment using the THM has observed three resonances in the energy regions below $E_{cm} \approx 450$ keV. These energies correspond to typical AGB temperatures, thus implying a significant increase in the reaction rate. Statistics are scarce for performing an accurate separation between resonances, preventing one from drawing a quantitative conclusion about their total widths and spin parities. Before THM measurement, only extrapolations were available below about 500 keV, showing a non-resonant behavior that sharply contradicts the trend of the astrophysical factor at higher energies. A new experiment has been performed to verify the measured TH astrophysical factor and to perform more accurate spectroscopy of the involved resonances.

Key words: nuclear reactions, nucleosynthesis, abundances

1. Introduction

Fluorine is an element with an uncertain and widely debated cosmic origin. It has only one stable isotope, ^{19}F, whose production and destruction is strictly connected to the physical conditions in stars. For this reason, fluorine abundances will place a severe constraint not only on chemical evolution models describing different stellar populations, but also on stellar evolution models (Jonsson et al. 2014).

Several sites and mechanisms for the Galactic production of fluorine have been proposed: during a type II supernova (SNeII) core-collapse through the neutrino spallation process (Woosley & Haxton 1988), in Wolf–Rayet (W–R) stars via helium burning and then ejection into the interstellar medium through stellar winds (Meynet & Arnould 2000), and in the low- and intermediate-mass asymptotic giant branch (AGB) stars during the He-burning thermal pulses (TP) and the subsequent third dredge-up episodes (Cristallo et al. 2009). In addition to these scenarios, fluorine can be produced during white dwarf mergers forming hydrogen-deficient stars with high carbon and fluorine abundances (Longland et al. 2011). However, the contribution by this process compared to the others is small because only few stars of this type are known compared to the AGB stars, SNeII, and WR stars (Jonsson et al. 2017). The origin of this element and contributions from the above-mentioned sources is still rather uncertain.

The relative importance of these production sites has not been established even for the solar neighborhood, leading to uncertainties in stellar evolution models of AGB stars as well as to uncertainties in the chemical evolution models of stellar populations (Jonsson et al. 2014).

While some papers have excluded the first two scenarios (the production of fluorine by the neutrino process because we lack any evidence for this in the interstellar medium (Federman et al. 2005) and the fluorine production of W–R stars has been theoretically questioned by Palacios et al. (2005), recent studies underline the equal importance of both possibilities (Kobayashi et al. 2011; Jonsson et al. 2014).

To date, direct proof of fluorine production in all the proposed scenarios has only been found in AGB stars via observations: by direct measurements of fluorine abundance in AGB stars (Jorissen et al. 1992; Abia et al. 2009, 2010, 2015), and by measurements of fluorine in post-AGB stars and planetary nebulae (Zhang & Liu 2005; Otsuka et al. 2008) as well as in carbon-enhanced metal-poor stars (Lucatello et al. 2011) and Ba stars (Alves-Brito et al. 2011). In addition, fluorine pollution by AGB stars in globular clusters has been shown by, for example, D'Orazi et al. (2013).

AGB stars are among the most significant polluters of the interstellar medium (Cristallo et al. 2014). In fact, they eject both light (C, N, F, Na) and heavy elements. This is the consequence of the alternating action of nuclear burning and

deep convective mixing episodes taking place during the thermally pulsing AGB (TP-AGB) phase. The presence of free neutrons in the He-rich intershell of these stars, which is required for synthesizing elements heavier than iron, also affects the light element nucleosynthesis and, among others, fluorine. In fact, in AGB stars fluorine can be produced via the chains ^{14}N(α, γ)^{18}F(β^+)^{18}O(p, α)^{15}N(α, γ)^{19}F, where neutrons and protons come from the reactions ^{13}C(α, n)^{16}O and ^{14}N(n, p)^{14}C, respectively. Thus, the production of F essentially depends on the amount of ^{13}C available in the He-rich intershell, but also on the availability of ^{13}C in the ashes of the H-burning shell (Jonsson et al. 2017).

It is not certain, however, that the fluorine produced by this process can account for the cosmic abundance (Jonsson et al. 2017). The production of fluorine from AGB stars may not be enough to explain the abundance of fluoride in the solar district (Abia et al. 2015).

Thus, the importance of ^{19}F in the study of AGB stars is twofold: on one hand, the understanding of fluorine nucleosynthesis in AGB stars is crucial to justify observed fluorine abundances, such stars being also established sources of galactic fluorine. On the other hand, the fluorine abundance observed in giant star can constrain models and heavy nucleosynthesis scenario since it is strictly connected to the mixing processes (standard and extra-mixing) taking place inside AGB stars (Jonsson et al. 2014).

The first systematic search of fluorine enhancements in AGB stars was made by Jorissen et al. (1992). This pioneering study showed very high ^{19}F surface enrichments (up to 30 times solar).

This occurrence was immediately interpreted as clear evidence of the fluorine synthesis by AGB stars. The highest values of the observed ^{19}F enhancements in the stellar atmosphere are not matched by standard AGB models and require additional mixing (Lugaro et al. 2004; Cristallo et al. 2009). However, reanalysis by Abia et al. (2009, 2010) of the same sample has reconciled theoretical models with observations. Indeed, at solar-like metallicities, the agreement between theory and observations is rather good. At lower metallicities, the situation is even more complex (Abia et al. 2015), since models predict larger enhancements than observed. The available determinations of F abundances in low-metallicity stars delineate a more intricate scenario than that provided from the easy theoretical scheme. For instance, the surface composition in a globular cluster, such as ω Cen, is hindered by the uncertain star formation and complex chemical enrichment history of this cluster; so it is not explained by a general model of other globular clusters (Li et al. 2013). In the case of CEMP-s stars (mostly binaries), the abundances measured might likewise be affected by the dilution of the accreted material onto the envelope of the secondary star. The amount of this material accreted is uncertain, as is consequently the interpretation of the abundances in general (Abia et al. 2015).

This discrepancy requires a revision of the nuclear reaction rates involved in the production and destruction of F in AGB stars. This might provide an alternative explanation for the know inconsistencies between model predictions and observations. The main fluorine destruction channels are ^{19}F(p, α)^{16}O and ^{19}F(α, p)^{22}Ne reactions.

The ^{19}F(α, p)^{22}Ne reaction, the main destruction channel in He-rich environment, has recently been studied in the astrophysical energy region by means of the Trojan horse method (THM) (Pizzone et al. 2017).

In this work we focus on the first reaction, the ^{19}F(p, α)^{16}O. In low-temperature, hydrogen-rich environments, which are characterized by a maximum temperature of about 10^7 K, the energy region below 500 keV is of key importance, thus the ^{19}F(p, α)^{16}O cross-section should be well determined at $E_{\rm cm}$ 50–300 keV for accurate modeling.

2. Available Direct and Indirect Data

The (p, α_0) channel (^{16}O being left in its ground state following ^{20}Ne decay) of the ^{19}F(p, α)^{16}O reaction dominates the total rate at temperatures relevant for AGB stars (Spyrou et al. 2000).

Until few years ago, the recommended low-energy values of the ^{19}F(p, α_0)^{16}O astrophysical factor $S(E)$ were collected in the Nuclear Astrophysics Compilation of Reaction Rates (NACRE) (Angulo et al. 1999), and came from several works: Breuer (1959) ($E_{\rm cm}$ = 461–684 keV, absolute data), Isoya et al. (1959) ($E_{\rm cm}$ = 598–1385 keV, data normalized by assuming σ = 42 mb at $E_{\rm cm}$ = 1.3 MeV), Caracciolo et al. (1974) ($E_{\rm cm}$ = 760–817 keV, absolute data), and Cuzzocrea et al. (1980) ($E_{\rm cm}$ = 1476–2544 keV, absolute data). The $S(E)$ factor shows about 10 resonances below 1 MeV, but direct measurements collected in NACRE stop at about 500 keV in the center-of-mass system (Breuer 1959), well above the relevant astrophysical range. In the range $0.6 < E_{\rm cm} < 1$ MeV, the data from Isoya et al. (1959) are in good agreement with data from Caracciolo et al. (1974), but disagree at lower energies with older measurements in Breuer (1959). Below $E_{\rm cm} \approx 460$ keV, however, only the unpublished data of Lorentz-Wirzba (1978) exist. These data extend to ≈150 keV bombarding energy and support a strong suppression of compound ^{20}Ne decay to the ground state of ^{16}O at $E_{\rm cm} \approx 0.14$–0.6 MeV. However, these results were not included in the NACRE compilation as possible systematic errors might have affected the absolute normalization (Angulo et al. 1999).

The astrophysical factor was then extrapolated to low energies assuming a dominant contribution of the non-resonant part (Angulo et al. 1999), supported also by the unpublished data. This conclusion disagrees with older measurements of Breuer (1959) that claimed the occurrence of two resonances at around 400 keV. The rate for $T_9 < 0.3$ was then determined mainly by the non-resonant (p, α_0) channel, causing a progressive increase of the uncertainties up to 50% at the lowest temperatures (Angulo et al. 1999). This very simple available non-resonant extrapolation to astrophysical energies suggested a nuclear origin of the disagreements observed in Galactic fluorine studies.

The unsatisfactory extrapolation and the persisting unsettled astrophysical issues triggered both indirect and direct new measurements focusing on the dominant α_0 channel.

The ^{19}F(p, α_0)^{16}O $S(E)$- factor at astrophysical energies was first investigated by means of the indirect THM, applied to the quasi-free (QF) ^{2}H(^{19}F, α_0^{16}O)n reaction induced at a beam energy $E_{\rm beam}$ = 50 MeV (La Cognata et al. 2011). This THM investigation allowed for spanning a p–^{19}F relative energy interval from 0 to about 1 MeV, completely overlapping the one of astrophysical interest, which also covers the region below 450 keV, where only extrapolations were available.

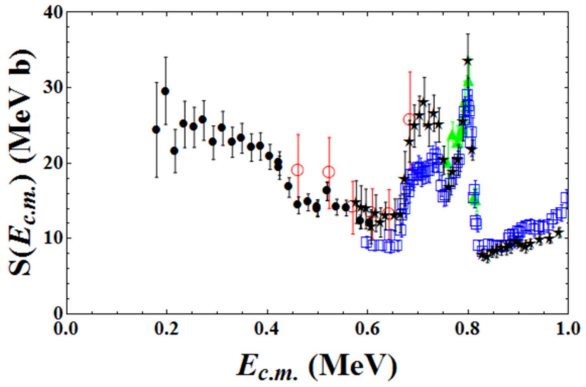

Figure 1. Available direct data for the ^{19}F(p, α_0)^{16}O reaction. The empty red circles show the data of Breuer (1959), the empty blue squares the data of Isoya et al. (1959), the green triangles the data of Caracciolo et al. (1974), the black stars the data of Lombardo et al. (2013), and the black circles the data of Lombardo et al. (2015).

The measurement of the α_0 channel shows three resonances in the energy regions below $E_{\rm cm} \approx 450$ keV that have not been seen before. In particular, the 113 keV resonance ($E_{^{20}\rm Ne} = 12.957$ MeV, 2^+) could play a crucial role since it falls inside the Gamow energy region.

However, the THM investigation of La Cognata et al. (2011) suffers of statistic and energy resolution effects. These effects did not allow us to achieve a good separation between resonances, which prevented an accurate estimate of the their total widths as well as the reaction rate.

Later, new direct data were made available in the normalization energy region (Lombardo et al. 2013). As shown in Figure 1, in the energy region $E_{\rm cm} > 0.7$ MeV, the new results agree with the data included in the NACRE compilation. Below 0.7 MeV, the data of Lombardo et al. (2013) are in agreement with those by Breuer (1959), which are larger by a factor of about 1.4 than the data from Isoya et al. (1959).

Thanks to the most recent data of Lombardo and because THM measurements need a normalization to high-energy direct data, the data of Lombardo et al. (2013) were used to normalize the THM data of La Cognata. This reanalysis was needed in order to asses the THM result thanks to the most and accurate measurements of Lombardo et al. (2013) with respect to those of Isoya that were originally used in La Cognata et al. (2011).

Thus, the THM data were normalized to the more recent and accurate astrophysical factor of Lombardo et al. (2013) to verify the dependence of the THM astrophysical factor on normalization when more than one peak was used (La Cognata et al. 2015). The contribution of the 113 keV resonance is the same in both works, and very good agreement is found between the resonance energies and widths in La Cognata et al. (2011) with those reported by Lombardo et al. (2013); this is a further test of the robustness of the THM even in the case of direct data of questionable quality.

Regarding direct measurements of this channel, new data have been provided by Lombardo et al. (2015) in the $E_{\rm cm} \approx 0.2$–0.6 MeV energy interval. The smooth increase of $S(E)$ in this energy region suggests the possible existence of resonances at $E_{\rm cm} < 300$ keV. However, their uncertainties are still too large below 0.2 MeV, and data need to be better constrained to draw astrophysical considerations.

More indirect measurements are necessary to further validate the present data. In fact, Lombardo et al. (2015) reported new spectroscopic information and an important contribution from the 0.251 MeV resonance. This resonance was not included in La Cognata et al. (2011). Indeed, due to the low-energy resolution, it was difficult to resolve the contributions of the 0.204 and 0.251 MeV resonances, and the low statistics did not allow us to deduce angular distributions to correctly attribute spin parities. Considering these factors and the complex ^{20}Ne spectroscopy characterized by several levels in this region, the 0.204 MeV was assumed to be dominant because of its higher spin.

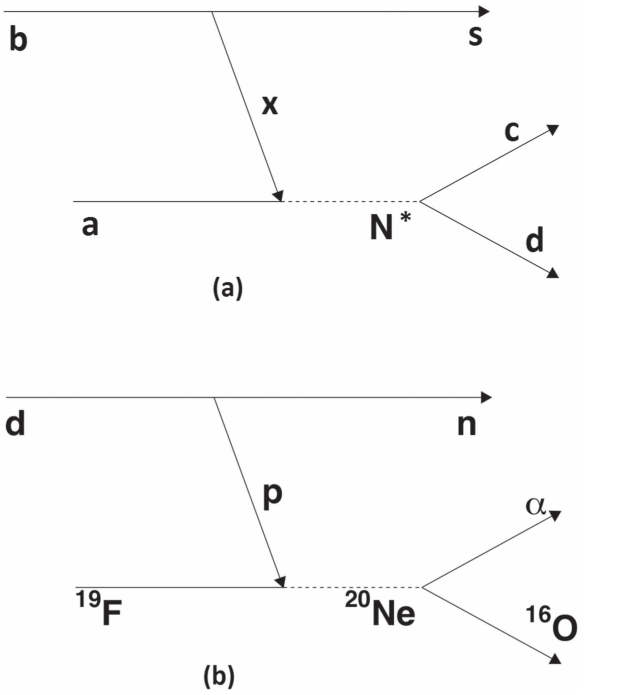

Figure 2. (a) Schematic view of the TH reaction $b + a \rightarrow c + d + s$ in the QF kinematics, proceeding through the formation of the $N^* = c + d$ resonant state. (b) Schematic diagram representing the ^{2}H $+^{19}$ F $\rightarrow \alpha +^{16}$ O $+ n$ QF process. The upper vertex describes the virtual decay of the THM-nucleus ^{2}H into the participant p and spectator n and the $p +^{19}$ F $\rightarrow \alpha +^{16}$ O reaction that takes place in the lower vertex.

A new THM experiment has been performed to improve the energy resolution and perform more accurate spectroscopy of the involved resonances, to check the compatibility of THM data with the direct data, and to reach a more complete understanding of the low-energy behavior of the S-factor.

3. The Trojan Horse Method

The THM (Baur 1986; Spitaleri 1991; Spitaleri et al. 2011, 2016; Tribble et al. 2014) is an indirect technique through which reactions of astrophysical relevance can be measured down to the Gamow-peak energy region with high precision and accuracy. A three-body reaction is performed at a beam energy that allows us to overcome the Coulomb barrier in the reaction entrance channel as well as the electron screening due to atomic electrons. The THM has been successfully applied to a number of reactions (see, for instance, Tribble et al. (2014) and references therein), and the method has recently been proven suitable for measurements involving radioactive ion beams (Cherubini et al. 2015; Pizzone et al. 2016) and neutrons (Lamia et al. 2008; Gulino et al. 2013; Guardo et al. 2017), thus proving its wide range of applicability.

By referring to Figure 2, the cross-section of the two-body reaction of interest in the THM approach

$$a + x \rightarrow c + d \quad (1)$$

is determined by properly selecting the quasi-free contribution of the three-body reaction

$$a + b \rightarrow c + d + s, \quad (2)$$

the nucleus b being chosen because of its $x \oplus s$ cluster structure. The beam energy is compensated for by the $x \oplus s$ binding energy so that the two-body reaction can take place at very low a–x relative energies, determining the so-called quasi-free two-body energy given by

$$E_{qf.} = E_{ab} - B_{x-s}, \quad (3)$$

where E_{ab} represent the beam energy in the center-of-mass system and B_{x-s} is the binding energy for the x–s system. Moreover, a single beam energy is required to obtain the full excitation function thanks to the x–s intercluster motion, allowing us to measure a wide range of a–x relative energies and to cover a wide c.m. angular range.

The reaction used in the THM can proceed through different reaction mechanisms. The TH reaction mechanism shown schematically in Figure 2 panel (a) gives the dominant contribution to the cross-section in a restricted region of the three-body phase space when the relative momentum of the fragments s and x is zero (the QF kinematical condition) or small compared to the bound state $x \oplus s$ wave number.

Particle x is virtual so the $a(x, c)d$ THM cross-section is half-off-energy-shell (HOES) and cannot be right juxtaposed to the direct (on-energy-shell, OES) cross-section. Thus, THM data need to be properly normalized to the direct data in order to obtain the results in absolute units.

In the case of resonant reactions, the modified R-matrix approach (La Cognata et al. 2011; Tribble et al. 2014) has been introduced. In the modified R-matrix framework, assuming that the reaction $a(x, c)d$ proceeds via isolated non-interfering resonances so that a one-level, two-channel R-matrix formula applies, the cross-section of the THM reaction in the plane wave impulse approximation (PWIA) can be written as

$$\frac{d^2\sigma}{dE_{xa}d\Omega_s} = NF\sum_i (2J_i + 1) \times \left| \sqrt{\frac{k_f(E_{xa})}{\mu_{cd}}} \frac{\sqrt{2P_{li}(k_{cd}R_{cd})}M_i(p_{xa}R_{xa})\gamma^i_{cd}\gamma^i_{xa}}{D_i(E_{xa})} \right|^2, \quad (4)$$

where NF is a normalization factor, $k_f(E_{xa}) = \sqrt{2\mu_{cd}(E_{xa} + Q)}/\hbar$ (Q is the reaction Q-value), P_{li} the penetration factor in l_i-wave, R_{xa} and R_{cd} the channel radii,

$$M_i(\rho_{xa}R_{xa}) = \left[(B_{xa_i} - 1)j_{l_i}(\rho) - \rho\frac{\partial_{jl_i}(\rho)}{\partial_\rho} \right]_{\rho=p_{xa}R_{xa}}, \quad (5)$$

where $j_{l_i}(\rho)$ is the spherical Bessel function, $p_{xa} = \sqrt{2\mu_{xa}(E_{xa} + B_{xs})}/\hbar$ (B_{xs} the binding energy of the $a = (xs)$ system), and B_{xa_i} an arbitrary boundary condition chosen to yield the observable resonance parameters. Finally, $D_i(E_{xa})$ is the standard R-matrix denominator in the case of one-level, two-channel R-matrix formulas (Lane & Thomas 1958).

In Equation (4), the OES and the HOES S-factors carry the same reduced widths, the only difference being the presence of Coulomb and centrifugal barrier penetrability in the OES $S(E)$ factor that is missing in the entrance channel of the HOES factor. Therefore, from the fitting of the TH cross-section, which is not affected by electron screening and by experimental energy resolution, the OES factor can be obtained and used to deduce the astrophysical factor.

Since in PWIA no absolute units are accessible, normalization is needed. It is obtained by scaling the deduced width of the THM measured resonances to those of direct data in the energy region where directly measurements are available. This, in turn, allows us to derive the THM data in absolute units in the energy region where no direct measurements are available.

The ^{2}H(^{19}F, α^{16}O)n three-body reaction has been chosen in order to extract the ^{19}F(p, α)^{16}O two-body cross-section, where deuteron is used as TH-nucleus to transfer the participant proton owing to its obvious p–n structure. A schematic view of the QF three-body reaction proceeding through deuteron break-up is reported in Figure 2 panel (b). In this figure the lower pole represents the virtual two-body reaction and the upper pole represents the break-up of deuteron used as TH nucleus. Since the relative motion of the neutron–proton system inside deuteron takes place essentially in s-wave ($l = 0$), and the QF break-up occurs in the target nucleus, the experimental momentum distribution is expected to be peaked at $p_s = 0$ MeV c^{-1} (Zadro et al. 1987; Lamia. et al. 2012). Under these hypotheses, the ^{19}F is considered to interact only with a part (proton) of the deuterium nucleus, while the other part (neutron) is considered a spectator to the ^{19}F(p, α)^{16}O virtual reaction. The experimental TH cross-section was analyzed in the modified R-matrix approach, which is discussed in La Cognata et al. (2013), to explore the energy region $E_{cm} \leqslant 1$ MeV.

4. The Experiment

The measurement was performed at the Laboratori Nazionali di Legnaro (Italy). The Tandem-XTU accelerator provided a 55 MeV ^{19}F beam with a spot size on target of 1 mm and intensities around 1–3 nA. Thin self-supported deuterated polyethylene targets (CD_2) of about 95 μg cm^{-2} were used to minimize energy and angular straggling, placed at 90° with respect to the beam direction.

A drawing of the experimental setup is given in Figure 3. It consisted of a telescope optimized for ^{16}O detection to distinguish oxygen nuclei via the ΔE–E technique. The telescope consists of an ionization chamber (IC) as ΔE stage and a silicon position-sensitive detector (PSD1) as E stage on one side with respect to the beam direction, and an additional silicon PSD on the opposite side optimized for coincident detection of alpha particles (PSD2). A symmetric setup allowed us to double statistics. Angles and distances for each PSD and IC are summarized in Table 1.

In order to minimize the angular straggling in PSDs, a 0.9 μm thick mylar foil was used as entrance window of the ICs; the opposite side was closed by a 1.5 μm thick Mylar foil. ICs were filled with 50 mbar butane gas that provided an energy resolution of about 10%, which was enough to distinguish the impinging particles according to their nuclear charge but not their mass. The four 1000 μm PSDs (5 × 1 cm^2)

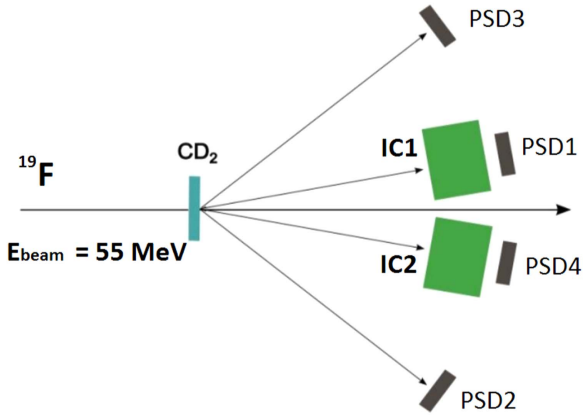

Figure 3. Sketch of the experimental setup, showing the ΔE–E system, consisting of an ionization chamber (IC) and a position-sensitive detector (PSD), devoted to ^{16}O detection, and a PSD on the opposite side with respect to the beam direction, optimized for alpha-particle detection.

Table 1
Detector Angles, Positions, and Thicknesses

	PSD1	PSD2	PSD3	PSD4	ICs
Center (degree)	15	46	46	15	15
Distance (cm)	23	18	18	23	16
Thickness (μm)	1000	1000	1000	1000	50000

have intrinsic energy and position resolution 0.5% and 0.3 mm, respectively, and cover the 8°–21° and 38°–54° angular range.

The adopted setup introduces an evaluated detection energy threshold of ∼6 MeV for ^{16}O nuclei. This does not constitute a problem for our experiments since detailed kinematical calculations show that ^{16}O nuclei coming from the ^{2}H+^{19}F interaction are expected with a lowest energy of 30 MeV; while a negligible threshold is introduced on the α-particle spectrum (spanning from 0 to 20 MeV) through dead layers in the detectors. So, to decrease the detection threshold, no ΔE detectors were placed in front of PSD2 and PSD3, therefore α-particle identification was made from kinematics.

Angular conditions were selected to maximize the expected QF contribution. The trigger for the event acquisition was given by coincidences between the telescopes and the signal coming from the other two PSDs. This allowed for the kinematical identification of our specific exit channel of reaction $d(^{19}\mathrm{F}, \alpha^{16}\mathrm{O})n$.

Energy and position signals for the detected particles were processed by standard electronics and sent to the acquisition system for online monitoring of the experiment and data storage for offline analysis.

5. Data Analysis

At the initial stage of the measurement, grids with a number of equally spaced slits were placed in front of each PSD to perform angular calibration. The central angle of each detector and the angle of each slit with respect to the beam direction was measured by means of an optical system, making it possible to establish a correspondence between position signal from the PSDs and detection angle of the impinging particles.

Energy detector calibration were performed by means of ^{16}O elastic and inelastic scattering in the energy range 30–60 MeV through the interaction with a gold and carbon target for PSD1 and PSD4. The calibration of PSD2 and PSD3 was performed by means of the same ^{19}F beam, by detecting the α particles from the $^{19}\mathrm{F}(p, \alpha)^{16}\mathrm{O}$ reaction induced onto a CD_2 target, performed at 55 MeV. A standard three-peak α-source was used to calibrate PSD2 and PSD3 at low energies.

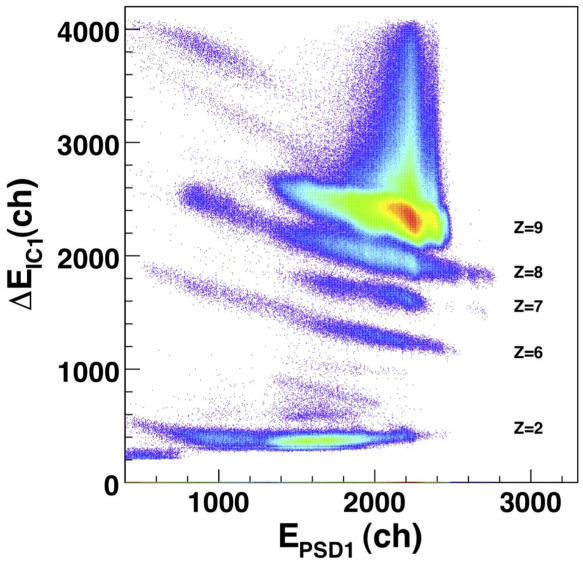

Figure 4. Particle ID with the standard ΔE–E technique in the ΔE_1–E_{PSD1} telescope. The symmetric telescope provides similar result.

In this way, calibrations are performed with the same particles we are interested in, which improves the accuracy of the calibration procedure. The ICs were calibrated by difference in the residual energy measured by PSDs when the ICs were empty and filled with 50 mbar isobutane gas. The total kinetic energy of the detected particles was reconstructed offline, taking into account the energy loss in the target and in the entrance and exit windows of the ionization chamber and in the other dead layers.

After detector energy and position calibration, the $^{2}\mathrm{H}(^{19}\mathrm{F}, \alpha_0^{16}\mathrm{O})n$ channel was selected by gating on the ΔE–E spectra.

Figure 4 shows that the contribution from scattered ^{19}F beam particles ($Z = 9$) is still separated from the $Z = 8$ locus of interest. The channel selection procedure begins with the separation of the oxygen locus by means of a graphical cut.

A further kinematic selection of the reaction channel is required because the reaction products are well distinguished in Z but not in A because the energy resolution of the ionization chamber is quite poor.

After the selection of oxygen-isotopes, the channel reaction selection was performed. For this reason, the complete kinematic was reconstructed in the hypothesis that the third (undetected) particle s was a neutron by using momentum-energy conservation laws. To validate our assumption about the mass of the undected particle, the experimental procedure of Costanzo et al. (1990) was followed. Since the spectator momentum is deduced from the energies and emission angles of particles c and d by applying the momentum conservation equation, the variable $X = \frac{p_s^2}{2\mu}$ is independent of the mass of the undetected fragment s (u being the unit mass in a.m.u.). When we define $Y = E_{\mathrm{beam}} - E_c - E_d$, the energy conservation equation can be cast in the form

$$y = \frac{1}{A_s}x - Q_{2\to 3}, \tag{6}$$

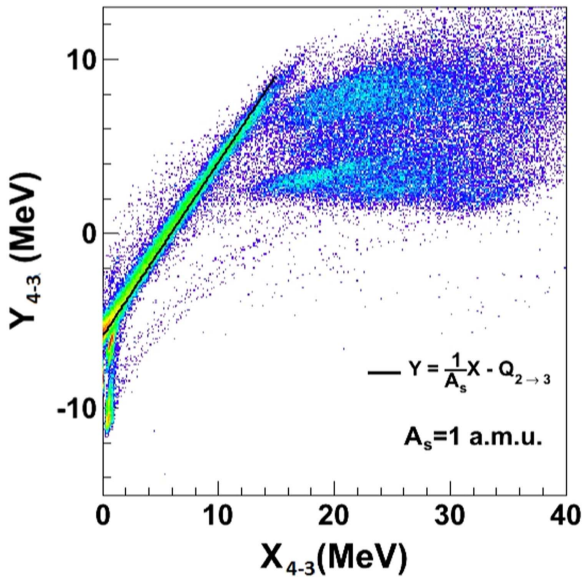

Figure 5. Identification of particle s according to the procedure of Costanzo et al. (1990), applied to the PSD3–PSD4 coincidences. The red line is calculated assuming $A_s = 1$ and a theoretical Q-value $Q_{2\to3} = 5.889$ MeV. Events gather along this line, attesting that they are emitted in reactions where a particle of unit mass is emitted, with a Q-value in agreement with the theoretical value.

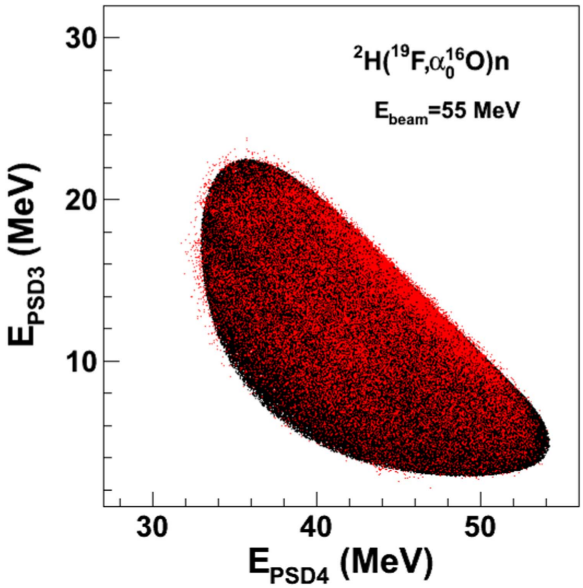

Figure 6. Kinematic locus of the ^{2}H(^{19}F, α_0^{16}O)n reaction. E_{PSD3} and E_{PSD4} are the energies of the particles detected in PSD 3 and 4, respectively, including the energy loss in dead layers and in the ΔE detector. The experimental data (red points) are compared here with simulated data for the ^{2}H(^{19}F, α_0^{16}O)n reaction channel (black points).

thus the mass of particle s can be inferred by fitting the line that best reproduces the experimental data. Therefore, this test allows for a comparison of the expected locus (a straight line) with the experimental locus, and it establishes the mass of s with no need of measurement. Indeed, events from reactions where a wrong identification of the detected ejectiles is carried out do not gather along a straight line because Equation (6) does not apply.

In this case, the events corresponding to the ^{2}H(^{19}F, α_0^{16}O)n reaction should gather around the straight line of the equation

$$y = x - 5.889, \tag{7}$$

the unity slope being due to $A_s = 1$. Figure 5 demonstrates that the locus of the ^{2}H(^{19}F, α_0^{16}O)n three-body reaction is well reproduced by the line of Equation (6), and it can be distinguished from the other as they are well separated. To rule out that these additional channels contribute to the experimental kinematical loci, a graphical cut was introduced in Figure 5 in order to remove the contaminating events.

Gating on such locus, energy correlation spectra were constructed for each angular couple and compared with the simulated spectra to single out the kinematic locus for the ^{2}H(^{19}F, α^{16}O)n 2 $\rightarrow$ 3 body reaction. In the simulations, $A = 16$ and $A = 4$ were assumed for the particles detected in coincidence.

Moreover, the Monte Carlo simulation took into account detection thresholds and energy losses in the dead layers.

The resulting total kinematic locus of the three-body reaction is reported in Figure 6, displaying the experimental kinematical locus (red point) as compared with the kinematical calculations (black points). Clearly, no contaminating kinematics overlap, namely no additional channels contribute to the experimental kinematic locus.

To check for the presence of further background and to evaluate the accuracy of the performed calibrations, the

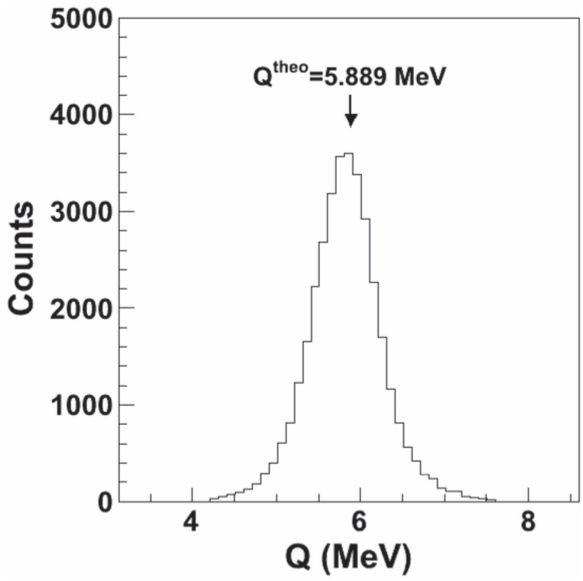

Figure 7. Q-value spectrum from the PSD3-4 coincidence for the events belonging to the $Z = 8$ locus in Figure 4 and situated along the red line in Figure 5. A single peak appeared, centered at the theoretical value, marked with an arrow. Similar results are obtained for the symmetric detector couple.

experimental Q-value spectrum was calculated for the events belonging to the ^{19}F+^{2}H kinematical locus, with the only hypothesis of a neutron as third particle, by imposing energy balance for the three-body reaction and compared with the theoretical one. It is shown in Figure 7, where the arrow demonstrates the theoretical Q-value for the ^{2}H(^{19}F, α_0^{16}O)n reaction. The presence of a single and symmetric peak, centered at an energy of about $Q_{3\text{-body}} = 5.889$ MeV, rules out the occurrance of significant systematic errors and confirms the correct identification of the reaction channel.

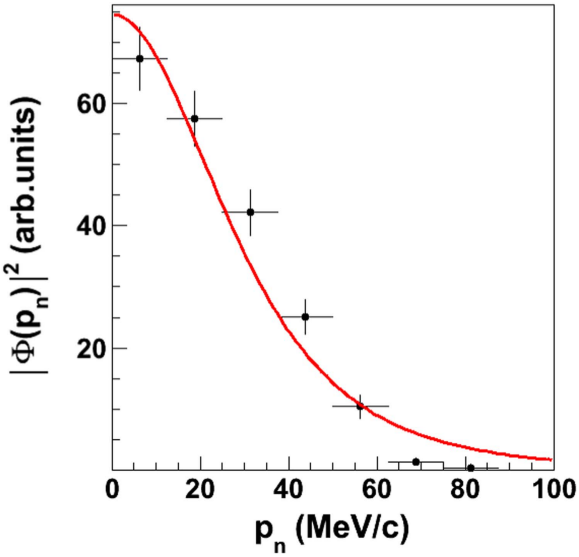

Figure 8. Experimental momentum distribution (full dots) extracted by selecting a E_{cm} relative energy windows of 300 keV and compared with theoretical distributions, given by the square of the Hulthèn wave function in momentum space (red solid line).

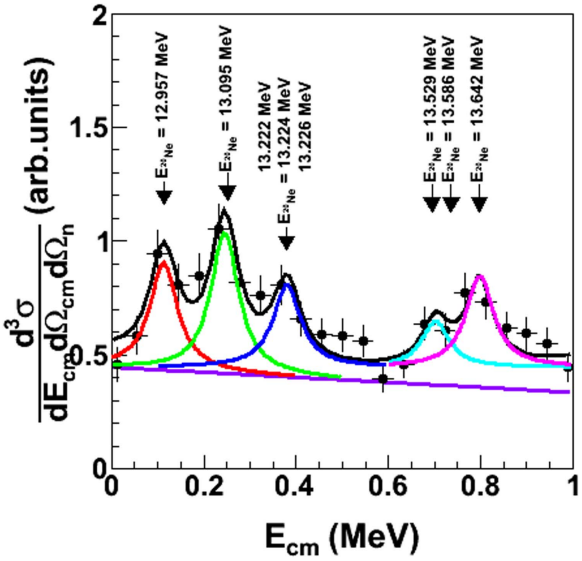

Figure 9. THM triple differential cross-section of the ^{2}H(^{19}F, α_0^{16}O)n reaction. The vertical error bars include the statistical uncertainty only. The horizontal error bars highlight the size of the integration bin. A multi-Gaussian fit has been used to distinguish the contribution of the resonances, marked by arrows, from the coincidence yield. The black line represents the sum of the contributions of the identified resonances.

Similar result are deduced from the symmetric pair of detectors. Thus, in the following, data analysis is restricted to such events.

The investigation of the experimental momentum distribution allows us to distinguish the sequential mechanism by introducing graphical selections that leave outside of the astrophysically relevant energy region events corresponding to sequential decays from intermediate compound nuclei. This step is of paramount importance for THM application since the equations shown in Section 3 apply only to the QF coincidence yield, thus data from other reaction mechanisms have to be rejected. To this purpose, a quantity that is very sensitive to the reaction mechanism leading to the population of the ^{2}H(^{19}F, α^{16}O)n channel is the momentum distribution of the p–n intercluster motion. If the mechanism is QF, the neutron momentum distribution keeps the same shape as inside deuteron. Thus, the agreement between the shape of the deuteron momentum distribution and the experimental distribution is compelling evidence of the occurrence of the QF mechanism.

The experimental momentum distribution was deduced by following the procedure described in Spitaleri et al. (2004), gating only the events belonging to the relative energy window of about 300 keV. The result of this procedure is displayed in Figure 8, and error bars include only the statistical error. It is compared with the expected theoretical one, given by the square of the Fourier transform of the radial bound-state wave function for the x–s system in the PWIA approach. In the case of deuteron, the theoretical distribution is given in terms of the squared Hulthèn wave function in momentum space:

$$\Phi = \frac{1}{\pi}\sqrt{\frac{ab(a+b)}{(a-b)^2}}\left[\frac{1}{a^2+p_s^2} - \frac{1}{b^2+p_s^2}\right], \qquad (8)$$

with parameters $a = 0.2317$ fm^{-1} and $b = 1.202$ fm^{-1} for the deuteron. The squared Hulthèn function in momentum space is superimposed onto the data in Figure 8 as a red line. Since the experimental momentum distribution was obtained in arbitrary units, selecting ^{19}F–p relative energy windows of a 300 keV, the theoretical distribution was scaled to the experimental maximum for comparison. The experimental full-width at half-maximum (FWHM) is 59 ± 10 MeV c^{-1}, in good agreement with the theoretical value of 58 MeV c^{-1}. Good agreement, within the error bars, is found between the experimental data and the theoretical Hulthèn function for the p–n motion inside the deuteron only in the $p_s < 30$ MeV c^{-1} range. This agreement represents a strong experimental evidence that the neutron acted as a spectator during the break-up that occurred in the ^{2}H(^{19}F, α_0^{16}O)n reaction. Since our equations work for QF kinematics only, in order to select the region corresponding to a dominant contribution of the QF-component, only events measured in coincidence for neutron momenta $p_s < 30$ MeV c^{-1} were considered in the forthcoming analysis, in agreement with the prescription given in Shapiro (1967), Spitaleri et al. (2011), and references therein.

Figure 9 shows the QF coincidence yield spectra obtained by selecting the ^{2}H(^{19}F, α_0^{16}O)n reaction channel as discussed and focusing on the $< p_s < 30$ MeV c^{-1} neutron momentum range to single out the QF contribution to the reaction yield.

The QF coincidence yield is plotted as a function of the ^{19}F–p relative energy E_{cm}, calculated through the equation

$$E_{cm} = E_{^{16}O-\alpha} - Q_2, \qquad (9)$$

where $E_{^{16}O-\alpha}$ is the relative energy between the outgoing α and ^{16}O particles and $Q_2 = 8.1136$ MeV is the Q-value of the ^{19}F(p, α_0)^{16}O reaction. The experimental spectra are corrected for phase space effects by dividing the coincidence yield by the simulated ^{19}F–p energy spectra, accounting for reaction kinematics, energy thresholds, and analysis cuts used to distinguish the QF contribution, modulated by the p–n momentum distribution.

In Figure 9 the selected events are shown as black points with their statistical error. The experimental data show a

Table 2
^{20}Ne Excited States Populated in the ^{19}F(p, α_0)^{16}O Reaction Adopted in the Present Work

$E_{^{20}\mathrm{Ne}}$ (MeV)	E_{cm} (MeV)	J^{π}	γ_p (MeV$^{1/2}$)	$\gamma_{\alpha 0}$ (MeV$^{1/2}$)	Γ_{α_0} (MeV)	$\Gamma_{\mathrm{TOT}}^{\mathrm{literature}}$ (MeV)	$\omega\gamma_0$ (eV)
12.957	0.113	2^+	0.110	0.068	0.038	0.038 ± 0.004[a]	1.25×10^{-6}
13.048	0.204	4^+	0.690	0.0446	0.010	0.018 ± 0.003[a]	3.71×10^{-6}
13.095	0.251	2^+	0.140	0.140	0.164	0.162 ± 0.013[a]	2.12×10^{-3}
13.222[b]	0.374	0^+	…	…	…	…	…
13.224[b]	0.376	1^-	…	…	…	…	…
13.226	0.378	3^-	0.150	0.086	0.054	0.053 ± 0.004[a]	13.26×10^{-3}
13.529	0.681	2^+	0.0983	0.088	0.07	0.061 ± 0.008[a]	13.04
13.586	0.738	2^+	0.0289	0.0399	0.014	0.010	1.97
13.642	0.794	2^+	0.051	0.0460	0.019	0.023[c]	5.7

Notes.
[a] The same reported in the compilation (Tilley et al. 1998).
[b] The contribution of this resonance is assumed to be negligible in the fitting.
[c] Data from Isoya (1959).

resonance at about $E_{\mathrm{cm}} \sim 113$ keV, which is due to the population of the 12.957 MeV excited level of ^{20}Ne ($J^{\pi} = 2^+$), a resonance at about $E_{\mathrm{cm}} \sim 251$ keV, which due to the population of the 13.095 MeV excited level of ^{20}Ne ($J^{\pi} = 2+$), a group of resonances, the dominant one being at about $E_{\mathrm{cm}} \sim 380$ keV, which is due to the population of the 13.226 MeV excited level of ^{20}Ne ($J^{\pi} = 3^-$), and three resonance at about $E_{\mathrm{cm}} \sim 696$, 739, and 798 keV, which are due to the population of the 13.529, 13.586, and 13.642 MeV excited levels of ^{20}Ne ($J^{\pi} = 2^+$). These were fit simultaneously with five Gaussian curves to separate the contribution from the normalized yield of each resonance. The fitting curves are shown in Figure 9. The red, green, and purple lines outline the contribution of the 12.975, 13.095, and 13.642 MeV ^{20}Ne levels, respectively, the blue line describes the combined yield of the 13.222, 13.224, and 13.226 MeV states, while the light blue line shows the contribution of the 13.529 and 13.586 levels. The black line is the sum of the obtained Gaussian functions. A violet line is used to denote the background. A single Gaussian was used in the cases of the 13.222, 13.224, and 13.226 MeV and in the 13.529 and 13.586 MeV levels since they could not be resolved in the experimental E_{cm} spectrum. The contribution of the background is well described by the violet line in Figure 9. The levels included in the fit are listed in Table 2. Excitation energies and spin parities are given.

The separation of the contribution of each resonance is important to integrate over the whole solid angle of the $d^3\sigma/dE_{\mathrm{cm}}\,d\Omega_{\mathrm{cm}}\,d\Omega_n$ cross-section and to eliminate background. The experimental yield shown in Figure 9 refers only to a θ_{cm} angular range, which is defined as the angle between the momentum of any of the two fragments (α or ^{16}O) and the virtual beam direction

$$\theta_{\mathrm{cm}} = \arccos(\hat{\boldsymbol{k}}_{p^{19}\mathrm{F}} \cdot \hat{\boldsymbol{k}}_{\alpha^{16}\mathrm{O}}). \tag{10}$$

In the previous formula, $\hat{\boldsymbol{k}}_{ij} = \frac{\boldsymbol{k}_{ij}}{k_{ij}}$ are the relative momenta between particles i and j. Since the experimental θ_{cm} range spans ~70°–120°, angular distributions outside this angular interval were calculated using the Blatt & Biedenharn (1952) standard formula. In the case of an isolated resonance with only one value of l_i, l_f, S_i, and S_f, it takes the form

$$\frac{d\sigma}{d\Omega}(\theta_{\mathrm{cm}}) = K(-1)^{S_f - S_i}\sum_L (\hat{l}_i)(\hat{l}_f)(\hat{J}_F)^2(-1)^L \begin{pmatrix} l_i & J_F & S_i \\ J_F & l_i & L \end{pmatrix} \times \langle l_i m_{li} l_i m_{li} | L M_L \rangle \begin{pmatrix} l_f & J_F & S_f \\ J_F & l_f & L \end{pmatrix} \times \langle l_f m_{lf} l_f m_{lf} | L M_L \rangle P_l(\cos\theta_{\mathrm{cm}}), \tag{11}$$

where $\begin{pmatrix} l_i & J_F & S_i \\ J_F & l_i & L \end{pmatrix}$ and $\begin{pmatrix} l_f & J_F & S_f \\ J_F & l_f & L \end{pmatrix}$ are Wigner 6j-symbols and $\langle l_i m_{li} l_i m_{li} | L M_L \rangle$ and $\langle l_f m_{lf} l_f m_{lf} | L M_L \rangle$ the Clebsch–Gordan coefficients.

The experimental THM angular distributions are shwon in Figure 10, where the different center-of-mass energies are marked for each picture. The angular distributions extracted are shown as red points, the direct data as black points, and the black line represents the theoretical prediction given by Equation (11). Thanks to the good agreement between our THM angular distribution and the theoretical distributions, the integration over the whole solid angle was performed. In more detail, using the formula in Equation (11), the ratio of the theoretical differential cross-section integrated over the experimental θ_{cm} angular range to the total cross-section was calculated:

$$\Xi_i = \frac{\int_{\theta_{\mathrm{cm}}^{\mathrm{min}}}^{\theta_{\mathrm{cm}}^{\mathrm{max}}} \frac{d\sigma}{d\Omega}(\theta_{\mathrm{cm}}) \sin\theta_{\mathrm{cm}}\, d\theta_{\mathrm{cm}}}{\int_0^{\pi} \frac{d\sigma}{d\Omega}(\theta_{\mathrm{cm}}) \sin\theta_{\mathrm{cm}}\, d\theta_{\mathrm{cm}}}. \tag{12}$$

Then, each resonance contribution to the THM cross-section, distinguished by means of the fits given in Figure 9, was divided by these factors to determine the angular integrated cross-section $d^2\sigma/dE_{\mathrm{cm}}d\Omega_n$. The THM cross-section integrated over the whole θ_{cm} range is displayed in Figure 11 in arbitrary units as black points.

The error budget affecting the experimental data accounts for statistical and angular integration uncertainties and background subtraction (vertical error bars). The horizontal error bars delimit the energy integration bins.

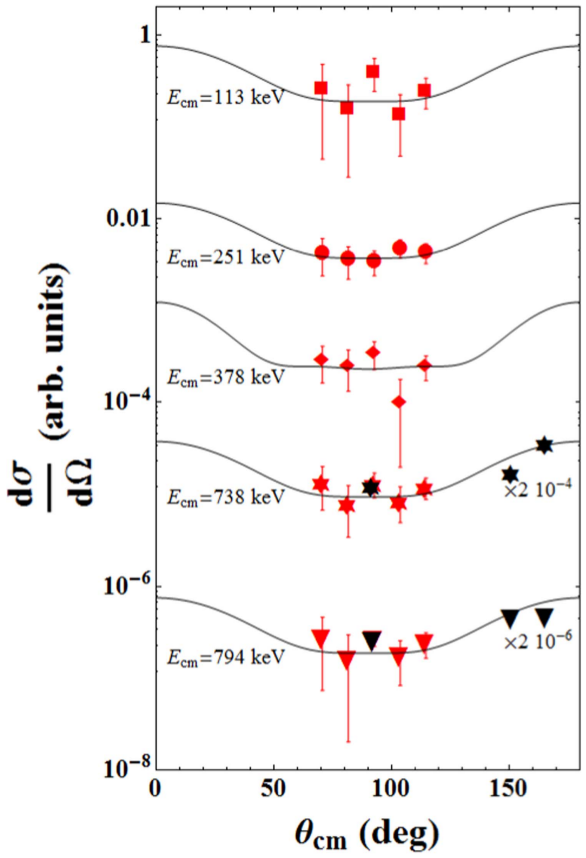

Figure 10. Angular distribution extracted at different E_{cm} via the THM (red point) compared to the direct data (black point) and the theoretical data (solid lines) (Breuer 1959; Dieumegard et al. 1980) calculated according to Equation (11).

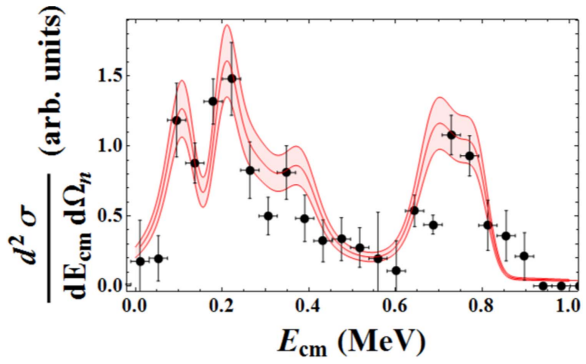

Figure 11. Cross-section calculated in the modified R-matrix approach. The black points are the experimental data, with the vertical error bars taking into account the statistical and angular distribution integration uncertainties and background subtraction. The red line represents the best fit to the data calculated in the modified R-matrix approach, normalized to the peaks at 681, 738, and 794 keV.

6. R-matrix Analysis

After we extracted the THM cross-section, we were able to determine the reduced widths of the involved resonant levels by means of Equation (4). Since the THM does not provide absolute values in its current formulation, it is mandatory to work out a normalization procedure.

Thus we focus on the region above 600 keV, where both direct and THM data are available. Normalization is obtained by scaling the THM $S(E)$ factor to fit the direct one in the energy range above 600 keV where the well known resonances at 681, 738, and 794 keV are dominant. When we use these input parameters in Equation (4) and also take the experimental FWHM resolution of 40 keV on the E_{cm} variable into account, the normalization factor NF appears as the only free parameters to adjust the HOES R-matrix calculation to the experimental THM data of Figure 11, expressed in arbitrary units.

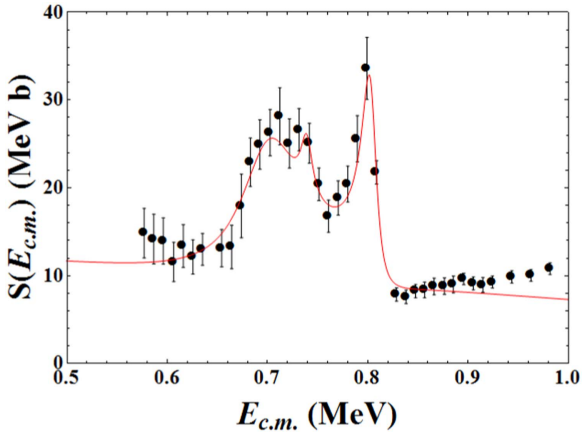

Figure 12. R-matrix fit (red line) of the $S(E)$-factor in Lombardo et al. (2013), shown with solid black symbols, performed using the same R-matrix code as in La Cognata et al. (2011).

As a first step, an R-matrix fit of the direct astrophysical factor data was performed using the R-matrix approach (see Lane & Thomas 1958 for more details). In the calculation, we chose to normalize THM data to the astrophysical factor of Lombardo et al. (2013) assuming a $J^{\pi} = 2^{+}$ for the 13.642 MeV ^{20}Ne state, and the non-resonant background in Lombardo et al. (2015) was adopted.

In Figure 12 the $S(E)$-factor from Lombardo et al. (2013) is shown as solid circles and the R-matrix fit performed using the same R-matrix code as in La Cognata et al. (2011) with a red line. Interference effects were fully taken into account, which justify the sharp drop of the astrophysical factor in the energy region above about 0.82 MeV.

After we fixed the NF, this scaled modified R-matrix calculation was needed to fit the THM resonances, thus allowing us to determine the reduced γ-widths, which were left as the only free parameters in the calculation. Equation (4) demonstrates that the same reduced widths appear in the modified and standard R-matrix equations, thus, the resonance parameters provided by fitting the experimental $d^2\sigma/dE_{cm}\,d\Omega_n$ cross-section were then introduced into a standart R-matrix code (Lane & Thomas 1958) to determine the astrophysical factor of the ^{19}F(p, α_0)^{16}O reaction at low energies.

The best fit of the THM corss section measured in this work is shown in Figure 11. The black points represent the experimental data of our work here, and the red middle line is the best-fit curve. The red band derives from the statistical error as well as the normalization to direct data from Lombardo et al. (2013).

Constructive interference was taken into account in the energy region between 0.113 and 0.251 MeV.

Energy and spin parity of these resonances were fixed to the values given in Lombardo et al. (2015). The resulting p- and α-reduced widths (γ_p and $\gamma_{\alpha 0}$) are given in Table 2.

The TH cross-section provided the resonance contribution only, thus the non-resonant part of the cross-section was taken from Lombardo et al. (2015).

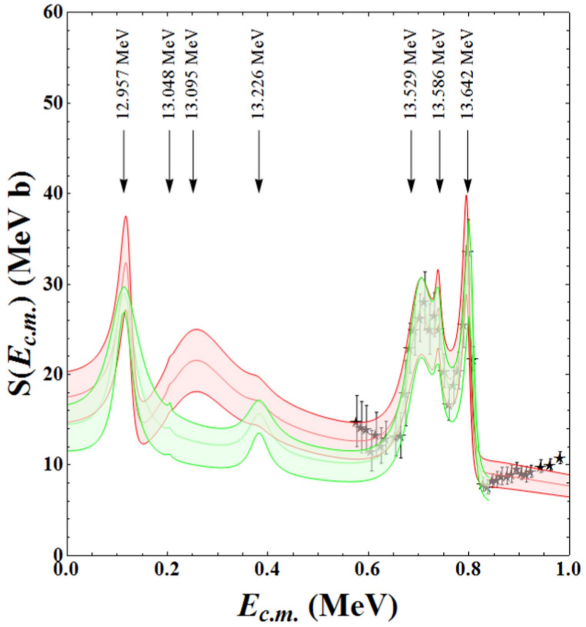

Figure 13. Comparison of the THM S-factor (red band) with the factors derived from previous indirect measurements (La Cognata et al. 2015) (green band). The red line shows the combination of the $S(E)$ factor from the fitting of Lombardo et al. (2013) data (above 600 keV) and of the one calculated using standard R-matrix formulae, where the resonance parameters where taken from the generalized R-matrix fitting of THM data below 600 keV. The black stars represent the experimental data from Lombardo et al. (2013). Finally, the arrows mark the ^{20}Ne states contributing to the $S(E)$-factor.

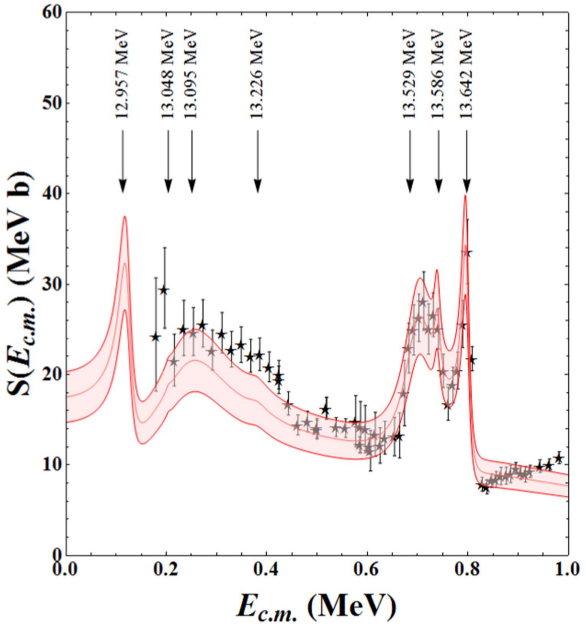

Figure 14. Comparison of the THM S-factor (red band) with direct data. The THM result is shown as a red band. The black stars represent the experimental data from Lombardo et al. (2013, 2015). Finally, the arrows mark the ^{20}Ne states contributing to the $S(E)$-factor.

Values of γ_p and $\gamma_{\alpha 0}$ parameters from the fitting of the THM HOES cross-section below 600 keV were then used to calculate the on-energy-shell ^{19}F(p, α_0)^{16}O astrophysical factor, shown in Figure 13. Above this energy, the resonance parameters are taken from the fitting of the data from Lombardo et al. (2013) for normalization. The middle red curve marks the $S(E)$-factor computed using the parameters from the best fit, while the red band arises from the uncertainties on the resonance parameters, which are due to the combined statistical and systematic error. In the same figure, data from Lombardo et al. (2013) are shown as stars.

For comparison, the THM $S(E)$-factor from La Cognata et al. (2015) was superimposed to the data and is shown as a green band. Both $S(E)$-factors were normalized to data of Lombardo et al. (2013) in the energy window 0.6–0.8 MeV.

The two $S(E)$-factor shows a large discrepancy in the energy region below 600 keV. The present $S(E)$-factor is higher than the factor shown in La Cognata et al. (2015), obtained with the same approach. The difference can be attributed to the 0.251 MeV resonance that is present in the S-factor deduced in this work and has not been observed in La Cognata et al. (2011, 2015).

In particular, the broad bump in the 0.2–0.4 MeV region is due to the constructive interference between the 0.113 and 0.251 MeV resonances. This resonance has not been included in the analysis of La Cognata et al. (2015) because the limited energy resolution did not allow us to distinguish the contribution of the 0.204 and 0.251 MeV, and the first resonance was assumed to be dominant because of its higher spin (4^+), as might be expected from the modified R-matrix formalism.

In Figure 14 the THM $S(E)$-factor of the ^{19}F(p, α_0)^{16}O reaction is compared with direct data from Lombardo et al. (2013, 2015). Figure 14 shows a good agreement between the THM $S(E)$-factor (red band) and the data in Lombardo et al. (2015) (black stars), within the error bars. As before, the middle red line is the best-fit curve, and the upper and lower red lines delineate the recommended range allowed by statistical, normalization, and data reduction uncertainties.

The reaction rate R was obtained using the astrophysical factor shown in Figure 13 by means of the standard equation

$$R_{ij} = \frac{N_i N_j}{1+\delta_{ij}}\langle \sigma v \rangle = \frac{N_i N_j}{1+\delta_{ij}}\left(\frac{8}{\pi A}\right)^{\frac{1}{2}}\left(\frac{1}{k_B T}\right)^{\frac{3}{2}} \cdot \int_0^\infty S(E)\exp\left[-\left(\frac{E}{k_B T} + 2\pi\eta(E)\right)\right]dE, \quad (13)$$

where N_i represents the number of nuclei of species i and the Kronecker symbol, $1+\delta_{ij}$ is introduced because otherwise, we would count each pair twice when $i=j$, k_B is the Boltzmann constant, T is the temperature,η is the Sommerfeld parameter, and E is the energy in the center-of-mass system. The reaction rate was calculated by introducing the THM astrophysical factor into Equation (13). The numerical values of the reaction rates are reported in Table 3, and it is parameterized with the fit function

$$R = \exp\left[0.36918 \times 10^2 + \frac{0.348699 \times 10^{-2}}{T_9} + - \frac{0.174149 \times 10^2}{T_9^{\frac{1}{3}}} - 0.144505 \times 10^2 \times T_9^{\frac{1}{3}} + + 3.82819 \times T_9 - 0.593586 \times T_9^{\frac{5}{3}} + + 1.68989 \times \ln(T_9)\right]. \quad (14)$$

The maximum percent difference from fit to value is about 10%.

Table 3
Recommended Values of the $^{19}F(p, \alpha_0)^{16}O$ TH Reaction Rate between $T_9 = 0.007$ and 5 and Its Ratio to the Rate Prescriptions in Angulo et al. (1999)

T_9	R_{α_0} (cm^3 mol^{-1} s^{-1})	$R_{\alpha_0}/R^{\rm nacre}_{\alpha_0}$
0.007	7.50993×10^{-29}	1.29068
0.009	1.26399×10^{-25}	1.29804
0.011	3.06779×10^{-23}	1.30545
0.013	2.2479×10^{-21}	1.31301
0.015	7.36394×10^{-20}	1.32077
0.018	4.94185×10^{-18}	1.33291
0.02	5.00128×10^{-17}	1.34141
0.025	5.16553×10^{-15}	1.36452
0.04	3.1254×10^{-11}	1.46036
0.05	1.26435×10^{-9}	1.56113
0.07	2.09108×10^{-7}	1.79345
0.09	6.14045×10^{-6}	1.85471
0.11	6.83326×10^{-5}	1.7529
0.14	9.51627×10^{-4}	1.57779
0.18	1.23676×10^{-2}	1.50449
0.2	3.47564×10^{-2}	1.51522
0.25	2.8003×10^{-1}	1.5767
0.3	1.35899	1.62195
0.35	4.69574	1.63543
0.4	1.28283×10^{1}	1.62571
0.45	2.96363×10^{1}	1.60291
0.5	6.05416×10^{1}	1.57404
0.6	1.95508×10^{2}	1.51247
0.7	5.01521×10^{2}	1.45443
0.8	1.10169×10^{3}	1.40167
0.9	2.16054×10^{3}	1.35343
1	3.88505×10^{3}	1.30898
1.75	7.35398×10^{4}	1.09541
2.5	4.01861×10^{5}	1.03268
3	8.52414×10^{5}	1.01881
4	2.27738×10^{6}	1.00838
5	4.11966×10^{6}	1.0048

The result is displayed in Figure 15 as a ratio to the NACRE α_0 reaction rate, calculated using the α_0 $S(E)$ factor recommended by NACRE (Angulo et al. 1999) by means of the standard formula in Equation (13). The calculation result is shown with a red line, while the red band highlights the region allowed by uncertainties (statistical, normalization, and data reduction) of about 16%.

It is evident that for temperatures $T_9 \sim 0.1$ ($T_9 = T/10^9$ K), temperature at which the ^{19}F destruction by extra-mixing process becomes more efficient, the present reaction rate is up to a factor of 2 higher than the rate calculated by Angulo et al. (1999). The enhancement is caused by the 113 keV peak in the $^{19}F(p, \alpha_0)^{16}O$ astrophysical factor.

This enhancement of the reaction rate can help solving the puzzle of fluorine nucleosynthesis in AGB stars since a larger ^{19}F destruction is expected by additional mixing processes.

The reaction rate given here essentially agrees with the rate from La Cognata et al. (2015) in the temperature range $0.04 \lesssim T_9 \lesssim 0.2$, as should be expected since the contribution of the 113 keV resonance is similar in both works, there is only a small difference ($\sim$10%) between the two.

$R_{\alpha_0}/R^{\rm nacre}_{\alpha_0}$ in Figure 15 significantly deviates from 1 at $T_9 \sim 0.4$ and is also 30% higher than the one suggested in La Cognata et al. (2015) and obtained with the same approach, but with a different identification of the 0.251 MeV level. The difference, in fact, is clearly due to the presence of the

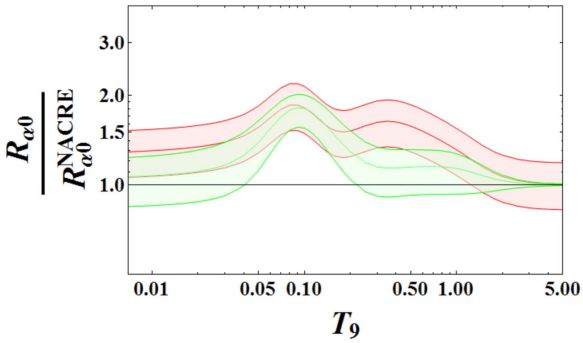

Figure 15. Ratio of the reaction rate calculation obtained from the THM astrophysical factor (red band) to the rate recommended in NACRE (Angulo et al. 1999). T_9 is the temperature in GK ($T_9 = T/10^9$ K). The black line corresponds to $R/R^{\rm nacre}_{\alpha_0} = 1$. For comparison, the $R/R^{\rm nacre}_{\alpha_0}$ ratio given in La Cognata et al. (2015) is shown as a green band.

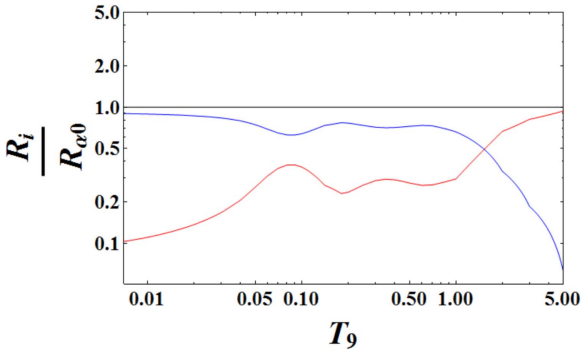

Figure 16. Ratio of the resonant (red line) and non-resonant (blue line) contributions to the THM (p, α_0) reaction rate (black line). The non-resonant part was taken from Lombardo et al. (2015).

0.251 MeV resonance and the effect of its interference with the 0.113 MeV level.

The relevance of the resonances in Table 2 is underlined in Figure 16, in which the ratios of the resonant and the non-resonant part to the THM α_0 reaction rate are shown. The blue line is used for the non-resonant contribution to the α_0 THM reaction rate. In the $0.007 < T_9 < 0.04$ range more than 90% of the contribution is due to the non-resonant part, but from $T_9 \approx 0.06$, the resonant part contributes by about 30% to the α_0 reaction rate. This enhancement is attributed to the 0.113 and 0.251 MeV resonances.

7. Evaluation of the $^{19}F(p, \alpha)^{16}O$ Reaction Rate

The $^{19}F(p, \alpha)^{16}O$ reaction rate is the sum over the rate for the (p, α_0), (p, α_1) and the (p, α_γ) channels. The reaction rate in Figure 15 refers only to the $^{19}F(p, \alpha_0)^{16}O$ channel that has been subject to the THM investigation, which to current knowledge should be dominant at very low temperatures. Indeed, from experimental data for the (p, α_0), (p, α_1), and (p, α_γ) channels, it turns out that the (p, α_γ) channel is dominant above about $T_9 \approx 0.5$ (Spyrou et al. 2000). However, from a close examination of the results in the literature, we can conclude that the available total reaction rates represent a lower limit only. In fact, while the (p, α_0) rate is well constrained by the present existing data, including the lowest energies, almost nothing is known from experiments on the (p, α_1) and (p, α_γ) rates at very low energies. Therefore, the error bar affecting the α_0 reaction rate in Figure 15 cannot be directly transferred to the total reaction rate, an unknown fraction of the total

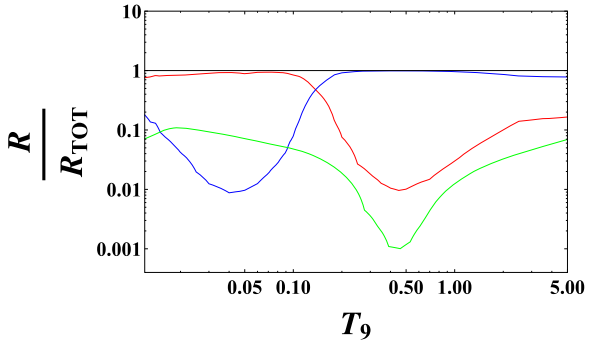

Figure 17. Contribution of each channel to the total reaction rate ($R_{\rm TOT}$). The black line corresponds to $R/R_{\rm total} = 1$. At very low temperatures, the (p, α_0) channel (red line) dominates the total rate. The (p, α_γ) channel (blue line) became dominant at least above $T_9 \approx 0.2$, while the (p, α_1) channel (green line) gives a maximum contribution of 10%.

cross-section being unconstrained. Indeed, the (p, α_1) data stop at about 600 keV (Angulo et al. 1999) and the (p, α_γ) data at $E_{\rm cm} = 188.8$ keV (Spyrou et al. 2000), leaving much space for unobserved resonances in the Gamow window for the AGB temperatures (between 0 and 200 keV). However, to emphasize the contribution of each channel to the total reaction rate, the data currently available in the literature were used to calculate the rate, and their ratios to the total reaction rate are shown in Figure 17. The black line is used for the $R/R_{\rm tot} = 1$, were $R_{\rm tot}$ is the total rate tabulated in Table 4 and calculated by adding to the contribution of the α_0-channel THM rate, the contributions of the α_1 and α_γ channels from Spyrou et al. (2000). The red line is used for the α_0 contribution, which is dominant only at lowest temperatures relevant for astrophysics ($0.007 < {\rm T9} < 0.15$), while the α_1 channel (green line) provides at most a 10% contribution to the total reaction rate. At higher temperatures, more than 90% of the contribution is due to the α_γ channel.

Moreover, in a stellar plasma, the excited levels of a target nucleus can be thermally populated and thus contribute to the reaction mechanism. So, the stellar rates may differ from those obtained when the target nuclei are in their ground state. This correction cannot be predicted on grounds of experimental data, except in very specific situations. This means that the stellar rates are not always constrained equally well because only the capture of the ground state of a target is measured in the laboratory. Therefore we must evaluate the thermalization effects through appropriate corrections factor whenever these effect are considered to be important (Angulo et al. 1999; Rauscher et al. 2011). In detail, at higher temperatures, the low-lying states in ^{19}F at 110 and 197 keV can be thermally populated, leading to a stellar enhancement factor and to a reduced ground-state contribution of the laboratory experiment (Rauscher et al. 2011).

As shown by NACRE (Angulo et al. 1999), the correction factor starts to be higher than 10% for $T_9 > 1$. Below, it is smaller than our error on the reaction rate, and therefore it can be neglected.

8. Conclusions

The fluorine abundance represents a strong constraint of the stellar internal structure because it is very sensitive to the physical conditions and mixing phenomena taking place in their inner layers (Lugaro et al. 2004; Jonsson et al. 2014).

Table 4
The ^{19}F(p, α_0)^{16}O TH Reaction Rate between $T_9 = 0.007$ and 5 and the ^{19}F(p, α)^{16}O Total Rate Calculated by Adding to the Contribution of the α_0-channel THM rate, the Contributions of the α_1 and α_γ Channels from Spyrou et al. (2000)

T_9	R_{α_0} (cm^3 mol^{-1} s^{-1})	$R_{\rm tot}$ (cm^3 mol^{-1} s^{-1})
0.007	7.50993×10^{-29}	…
0.009	1.26399×10^{-25}	…
0.011	3.06779×10^{-23}	…
0.013	2.24790×10^{-21}	2.86990×10^{-21}
0.015	7.36394×10^{-20}	9.13220×10^{-20}
0.018	4.94185×10^{-18}	5.94308×10^{-18}
0.02	5.00128×10^{-17}	5.96935×10^{-17}
0.025	5.16553×10^{-15}	5.93679×10^{-15}
0.04	3.12540×10^{-11}	3.34228×10^{-11}
0.05	1.26435×10^{-9}	1.42760×10^{-9}
0.07	2.09108×10^{-7}	2.22372×10^{-7}
0.09	6.14045×10^{-6}	6.75680×10^{-6}
0.11	6.83326×10^{-5}	8.64937×10^{-5}
0.14	9.51627×10^{-4}	2.1257×10^{-3}
0.18	1.23676×10^{-2}	8.837844×10^{-2}
0.2	3.47564×10^{-2}	4.5954×10^{-1}
0.25	2.8003×10^{-1}	1.04750×10^{1}
0.3	1.35899	7.58638×10^{1}
0.35	4.69574	3.70825×10^{2}
0.4	1.28283×10^{1}	1.22110×10^{3}
0.45	2.96363×10^{1}	3.08730×10^{3}
0.5	$6.0.5416 \times 10^{1}$	5.99823×10^{3}
0.6	1.95508×10^{2}	1.52381×10^{4}
0.7	5.01521×10^{1}	3.38758×10^{4}
0.8	1.10169×10^{3}	5.09114×10^{4}
0.9	2.16054×10^{3}	8.68438×10^{4}
1	3.88505×10^{3}	1.30554×10^{5}
1.75	7.35398×10^{4}	9.10733×10^{5}
2.5	4.01861×10^{5}	2.86877×10^{6}
3	8.52414×10^{5}	5.68102×10^{6}
4	2.27738×10^{6}	1.45×10^{7}
5	4.11966×10^{6}	2.48999×10^{7}

The problem is that current models fail to explain the highest F enhancements found in the lower metallicity AGB stars (Abia et al. 2015). A possible way to explain this abundance found in AGB star envelopes might be provided by a revision of the nuclear reaction rates involved in the synthesis of this nuclide in these stars. The ^{19}F(p, α)^{16}O reaction represents the main fluorine depleting channel in the low-temperature, hydrogen-rich environment.

In the case of extra-mixing phenomena, which are characterized by a maximum temperature of about 10^7 K (Pandey et al. 2008), the energy region below 500 keV is of key importance, thus the ^{19}F(p, α)^{16}O cross-section should be well determined at $E_{\rm cm}$ 50−500 keV for accurate modeling.

In particular, the α_0 channel, corresponding to the emission of α-particles off ^{20}Ne compound system leaving ^{16}O in its ground state, was investigated here because we considered it to be the larger contributor to the total cross-section.

Only one set of direct data is available at the energies $250 < E_{\rm cm} < 500$ keV, and no direct data are available at the energies $E_{\rm cm} < 250$ keV, where fluorine burning is most effective. The THM was thus used to access this energy region.

The present paper reported new experimental data of the ^{19}F(p, α_0)^{16}O channel in the energy range between 0 and 1 MeV throughout the THM, by extracting the quasi-free contribution to the ^{2}H(^{19}F, α_0^{16}O)n reaction, using the most

updated spectroscopic information on ^{20}Ne in the excitation energy region of interest.

To this purpose, the ^{2}H(^{19}F, α_0^{16}O)n reaction at 55 MeV beam energy was measured by means of a ^{19}F beam impinging onto deuterated polyethylene targets.

We used the modified R-matrix approach to investigate the energy region $E_{cm} < 1$ MeV, so as to span both the range of astrophysical interest and the $0.6 < E_{cm} < 0.8$ MeV interval needed for normalization. Thus, a fit of the direct $S(E)$ factor by Lombardo et al. (2013), down to about 0.6 MeV, was performed by means of standard R-matrix formulas.

Using Equation (4), we derived the reduced widths of the resonances in the 0–600 keV E_{cm} energy range.

Finally, after calculating the ^{19}F(p, α_0)^{16}O cross-section and its normalization to direct data, it was possible to calculate the reaction rate.

In the energy region around the E_{cm} 0.794 MeV resonance, the present results agree reasonably well with the data from previous experiments (La Cognata et al. 2011, 2015). In contrast, in the $E_{cm} < 0.6$ MeV energy range, the $S(E)$ factors extracted from new data show a large difference in comparison with the factor given in La Cognata et al. (2011, 2015) because of a 251 keV resonance.

The present results are in good agreement with the data extracted from Lombardo et al. (2015).

From the modified R-matrix calculation we calculated the reaction rate. We compared the present ^{19}F(p, α_0)^{16}O reaction rate with the rate reported in La Cognata et al. (2015). At the astrophysically relevant temperatures $T_9 = 0.04$–0.2, the rate from the present work agrees, within errors, with the rate obtained by La Cognata et al. (2015), and there is only a small difference ($\sim$10%) between the two adopted values. A larger discrepancy ($\sim$30%) is found at a temperature $T_9 \sim 0.4$ because of the interference of the 0.113 and 0.251 MeV resonances.

The main result of the present work is the estimate of the contribution of the 0.251 MeV level, as it is responsible for a bump in the energy region below 400 keV that extends to the region of astrophysical interest.

This work was supported by the Italian MIUR under Grants No. RBFR082838 and "LNS Astrofisica Nucleare (fondi premiali)."

References

Abia, C., Cunha, K., Cristallo, S., et al. 2009, ApJ, 694, 971
Abia, C., Cunha, K., Cristallo, S., & Laverny, P. 2015, A&A, 581, A88
Abia, C., Recio-Blanco, A., Laverny, P., et al. 2010, ApJL, 715, L94
Alves-Brito, A., Karakas, A. I., Yong, D., Meléndez, J., & Vàsquez, S. 2011, A&A, 536, 40
Angulo, C., Arnould, M., Rayet, M., et al. 1999, NuPhA, 656, 3
Baur, G. 1986, PhLB, 178, 135
Blatt, J. M., & Biedenharn, L. C. 1952, RvMP, 24, 258
Breuer, G. 1959, ZPhy, 154, 339
Caracciolo, R., Cuzzocrea, P., De Rosa, A., et al. 1974, Lett. Nuovo Cimento, 11, 33
Cherubini, S., Gulino, M., Spitaleri, C., et al. 2015, PhRvC, 92, 015805
Costanzo, E., Lattuada, M., Romano, S., Vinceiguerra, D., & Zadro, M. 1990, NucIM, 295, 373
Cristallo, S., Di Leva, A., Imbriani, G., et al. 2014, A&A, 570, A46
Cristallo, S., Straniero, O., Gallino, R., et al. 2009, ApJ, 696, 797
Cuzzocrea, P., De Rosa, A., Inglima, G., et al. 1980, Lett. Nuovo Cimento, 28, 515
Dieumegard, D., Maurel, B., & Amsel, G. 1980, NucIM, 168, 93
D'Orazi, V., Lucatello, S., Lugaro, M., et al. 2013, ApJ, 763, 22
Federman, S. R., Sheffer, Y., Lambert, D. L., & Smith, V. V. 2005, ApJ, 619, 884
Guardo, G. L., Spitaleri, C., Lamia, L., et al. 2017, PhRvC, 95, 025807
Gulino, M., Spitaleri, C., Tang, X., et al. 2013, PhRvC, 87, 12801
Isoya, A. 1959, NuPhA, 7, 126
Isoya, A., Ohmura, H., & Momota, T. 1959, NucPh, 7, 116
Jonsson, H., Ryde, N., Harper, G. M., Richter, M. J., & Hinkle, K. H. 2014, ApJL, 789, L41
Jonsson, H., Ryde, N., Spitoni, E., Matteucci, F., et al. 2017, ApJ, 835, 50
Jorissen, A., Smith, V. V., & Lambert, D. L. 1992, A&A, 261, 164
Kobayashi, C., Izutani, N., Karakas, A. I., et al. 2011, ApJL, 739, L57
La Cognata, M., Mukhamezhanov, A., Spitaleri, C., et al. 2011, ApJL, 739, L54
La Cognata, M., Palmerini, S., Spitaleri, C., et al. 2015, ApJ, 805, 128
La Cognata, M., Spitaleri, C., Trippella, O., et al. 2013, ApJ, 777, 2
Lamia., L., La Cognata, M., Spitaleri, C., et al. 2012, PhRvC, 85, 025805
Lamia, L., Spitaleri, C., Carlin, N., et al. 2008, NCim, 31, 423
Lane, A. M., & Thomas, R. G. 1958, RvMP, 30, 257
Li, H. N., Ludwig, H. G., Caffau, E., et al. 2013, ApJ, 765, 51
Lombardo, I., Dell'Aquila, D., Campajola, L., et al. 2013, JPhG, 40, 125102
Lombardo, I., Dell'Aquila, D., Di Leva, A., et al. 2015, PhLB, 748, 178
Longland, R., Lorén-Aguilar, P., José, J., et al. 2011, ApJL, 737, L34
Lorentz-Wirzba, H. 1978, PhD thesis, Univ. Munster
Lucatello, S., Masseron, T., Johnson, J. A., Pignatari, M., & Herwig, F. 2011, ApJ, 729, 40
Lugaro, M., Ugalde, C., Karakas, A. I., et al. 2004, ApJ, 615, 934
Meynet, G., & Arnould, M. 2000, A&A, 355, 176
Otsuka, M., Izumiura, H., Tajitsu, A., & Hyung, S. 2008, ApJL, 682, L105
Palacios, A., Arnould, M., & Meynet, G. 2005, A&A, 443, 243
Pandey, G., Lambert, D. L., & Kameswara Rao, N. 2008, ApJ, 674, 1068
Pizzone, R. G., D'Agata, G., La Cognata, M., et al. 2017, ApJ, 836, 57
Pizzone, R. G., Roeder, B., Mckluskey, M., et al. 2016, EPJA, 52, 24
Rauscher, T., Mohr, P., Dillmann, I., & Plag, R. 2011, ApJ, 738, 143
Shapiro, I. S. 1967, in Interactions of High-Energy Particles with Nuclei, ed. T. E. O. Ericson (New York: Academic Press), 210
Spitaleri, C. 1991, in Problems of Fundamental Modern Physics, II: Proceedings, ed. R. Cherubini, P. Dalpiaz, & B. Minetti (Singapore: World Scientific), 21
Spitaleri, C., La Cognata, M., Lamia, L., et al. 2016, EPJA, 52, 77
Spitaleri, C., Lamia, L., Tumino, A., et al. 2004, PhRvC, 69, 055806
Spitaleri, C., Mukhamezhanov, A., Blokhintsev, L., et al. 2011, PAN, 74, 1725
Spyrou, K., Chronidou, C., Harissopulos, S., et al. 2000, EPJA, 7, 79
Tilley, D. R., Cheves, C. M., Kelley, J. H., Raman, S., & Weller, H. R. 1998, NuPhA, 636, 249
Tribble, R. E., Bertulani, C., La Cognata, M., et al. 2014, RPPh, 77, 106901
Woosley, S. E., & Haxton, W. C. 1988, Natur, 334, 45
Zadro, M., Blagus, S., Miljaníc, Dj., et al. 1987, NuPhA, 474, 373
Zhang, Y., & Liu, X. W. 2005, ApJL, 631, L61